

Photoinduced reduction of surface states in Fe:ZnO

R. Knut,¹ U. Kvist,² P. Palmgren,¹ P. Pal,³ P. Svedlindh,⁴ A. Pohl,² and O. Karis¹

¹*Department of Physics and Astronomy,*

Uppsala University, Box 516, SE-751 20 Uppsala, Sweden

²*Department of Chemistry Ångström, Uppsala University,*

Box 538, SE-751 21 Uppsala, Sweden

³*MAX-lab, Lund University, Box 118, SE-221 00 Lund, Sweden*

⁴*Department of Engineering Sciences, Uppsala University,*

Box 534, SE-75121, Uppsala, Sweden

(Dated: August 26, 2018)

Abstract

Transition metal doping is known to increase the photosensitivity to visible light for photocatalytically active ZnO. We report on the electronic structure of nano-crystalline Fe:ZnO, which has recently been shown to be an efficient photocatalyst. The photo-activity of ZnO reduces Fe from 3+ to 2+ in the surface region of the nano-crystalline material. Electronic states corresponding to low-spin Fe²⁺ are observed and attributed to crystal field modification at the surface. These states can be important for the photocatalytic sensitivity to visible light due to their deep location in the ZnO bandgap. X-ray absorption and x-ray photoemission spectroscopy suggest that Fe is only homogeneously distributed for concentrations up to 3%. Increased concentrations does not result in a higher concentration of Fe ions in the surface region. This is a crucial factor limiting the photocatalytic functionality of ZnO, where the most efficient doping concentration have been shown to be 2-4% for Fe doping. Using resonant photoemission spectroscopy we determine the location of Fe 3d states with sensitivity to the charge states of the Fe ion even for multi-valent and multi-coordinated Fe.

I. INTRODUCTION

The photo-activity of ZnO is well known and the photocatalytic efficiency of this semiconductor can in some cases exceed that of TiO_2 ¹⁻³, which has been well studied for its photocatalytic properties. ZnO is therefore considered a low cost and environmentally friendly alternative to TiO_2 . Potential applications such as photocatalytic conversion of organic pollutants in water by the production of hydroxyl radicals and the splitting of water into H_2 and O_2 have been proposed.⁴⁻⁸ The photo-activity is also demonstrated by the transformation from hydrophobicity to hydrophilicity when these materials are subjected to UV light.⁹⁻¹³ Applications such as anti-fogging and self-cleaning windows have been realized utilizing this functionality.

Both ZnO and TiO_2 are wide bandgap semiconductors, which require UV light for photocatalysis to occur. However, for high photocatalytic efficiency from sun light, the responsiveness to lower photon energies needs to be developed. Therefore, doping the semiconductors with metal or non-metal atoms as well as mixing them with small bandgap semiconductors have been proposed for increasing the susceptibility to visible light.^{14,15} Several different transition metal dopants (Ni, Co, Mn and Cu) in ZnO have been studied for this purpose.^{6,14,16} Co doping appears to be most efficient and low doping concentrations (< 3%) are generally most effective, an additional thermal diffusion of Co to the surface have been shown to increase the photocatalytic activity.^{17,18} Transition metal doping have also been shown to enhance the photoinduced hydrophilicity in TiO_2 ¹⁹, it has been proposed that either an increased amount of oxygen vacancies or an enhanced photocatalytic activity is responsible for this effect.^{9,20} Several ferrite compounds have successfully been applied in visible light when mixed with TiO_2 , where maximum efficiency appears at low ferrite concentrations (1 - 3%).^{5,21-23} Efficient hydrogen generation have been demonstrated for $\text{ZnFe}_2\text{O}_4/\text{SrTiO}_3$.²⁴ Also, studies with Fe_3O_4 , Fe_2O_3 and ZnFe_2O_4 mixed with ZnO have been reported but has to date only been tested in the UV regime.^{5,25-27} In addition to the previously mentioned TM dopants, Fe doping of ZnO for visible light sensitizing has recently been reported.²⁸⁻³⁰

Since catalytic processes effectively occur on surfaces it is important that the characterization methods are not representative of the bulk, which can have a very different chemical and structural composition. For details on the chemistry of ZnO surfaces we refer to a review by Wöll.³¹ We present an extensive study of the surface composition and electronic

structure of Fe:ZnO by x-ray absorption and x-ray photoelectron spectroscopy.

II. EXPERIMENT

We have studied Fe:ZnO with Fe in the concentration range 1-10% by means of x-ray diffraction (XRD), Raman spectroscopy, transmission electron microscopy (TEM), SQUID magnetometry, x-ray photoemission spectroscopy (XPS) and x-ray absorption spectroscopy (XAS). The XRD, Raman spectroscopy, TEM and SQUID studies will be presented elsewhere, together with the details of the sol-gel synthesis.³² The Fe:ZnO films were prepared from stoichiometric solutions by repeated spin-coating on Si [100] substrates with a 300 nm native oxide termination. After deposition, the films were annealed in air at 600°C for 5 minutes. The resulting thickness of the ZnO:Fe films is about 1 μm . Thin film x-ray diffraction data did not indicate the existence of any secondary phases, but rather a phase pure wurtzite ZnO. However, Raman spectroscopy and TEM show the presence of an amorphous $\text{Zn}_x\text{Fe}_y\text{O}$ phase. Characterization using scanning electron microscopy revealed that the films are polycrystalline with the grain size continuously decreasing from 25 nm for 1% Fe to 10 nm for 10% Fe.

Here we will focus on the electronic structure obtained by XPS and XAS measurements which were performed at the bending magnet beamline D1011 at the MAX-lab facility in Lund, Sweden. The synchrotron measurements were performed during three different occasions with the same samples. For the first set of measurements the samples were heated to 220°C before valence band (VB) XPS, Fe 2p XPS and resonantly excited XPS characterizations were performed. For the second round of experiments, the samples were also heated to 220°C, prior to measuring Fe $L_{2,3}$ absorption. During the last round of measurements, O 1s and C 1s XPS were performed before as well as after heating to 220°C. The heating was performed *in-situ* for desorbing surface adsorbates.

III. RESULTS AND DISCUSSION

A. Valency of Fe at the surface and in the bulk

The Fe 2p XPS spectra of Fe:ZnO, presented in Fig. 1, are normalized to the same peak intensity for clarity. The spectra are collected with a photon energy of 1050 eV and are

energy calibrated relative to the Zn 3d peak for all Fe concentrations. The energy position of the Zn 3d peak for the 2% sample is calibrated to an Au Fermi edge in electrical contact with the sample. A Fe 2p XPS spectrum of BiFeO₃ obtained using 4 keV photon energy is also included in Fig. 1 as a reference of Fe³⁺ with octahedral coordination, denoted as Fe_{oct.}³⁺. This spectrum is also energy calibrated to the Fermi level. This sample has a satellite structure, indicated by the arrow, which is absent in the Fe:ZnO spectra. The satellite structure is typical for Fe³⁺.³³⁻³⁵ It is commonly accepted that the main peak of Fe²⁺ and Fe³⁺ involves a charge transfer from the ligand with the final states 2p⁵3d⁷L and 2p⁵3d⁶L respectively where L denotes an O 2p ligand hole. The satellite for Fe³⁺ comes from a 2p⁵3d⁶ final state without charge transfer from the ligand.³⁵ Even though the Fe 2p binding energy (BE) can differ between compounds the relative BE between the satellite and the main peak can be used as a fingerprint for the valency of Fe. In Fig. 1 none of the Fe:ZnO spectra show any distinct satellite structure between the 2p_{3/2} and 2p_{1/2} spin-orbit split components. This corresponds well to a mixed Fe³⁺/Fe²⁺ state.³⁶ The reason for this mixed valency is due to a reduction of Fe³⁺ as the sample is subjected to soft x-rays. To obtain reasonable quality spectra, as in Fig. 1, a data collection time of about 40 min is necessary. However, XAS is better adapted for studying the effect of x-ray induced reduction since a spectrum takes only a few minutes to collect.

For the XAS of Fe L₃ a full absolute photon energy calibration was obtained for the 1% and 10% Fe samples. Other samples were shifted to fit with the main peak of the 10% Fe sample. XAS of Fe L₃ for 2% Fe:ZnO is shown in Fig. 2. The absorption of Fe²⁺ is expected just above 708 eV (left arrow), while the Fe³⁺ is expected just below 710 eV (right arrow). The dashed black line indicates the position of Fe³⁺ in octahedral coordination obtained from a BiFeO₃ sample. The data were obtained with the same instrumental broadening as for the Fe:ZnO samples. Usually Fe prefers to order in octahedral coordination and therefore it is difficult to find reference data for purely tetrahedrally coordinated Fe. It has been suggested that the absorption of Fe_{tet.}³⁺ is very similar in spectral structure but situated around 0.3 - 0.8 eV below Fe_{oct.}³⁺ and for high-spin Fe_{tet.}²⁺ there are calculations which suggest that it is almost identical to Fe_{oct.}²⁺.^{37,38} We will therefore omit the subscript (oct. and tet.) for the Fe²⁺ components. The 2% sample was additionally heated to 400°C in vacuum after which it was subjected to air (red dashed line). This treatment has oxidized the sample which now shows an almost pure Fe³⁺ character after short x-ray exposure. This

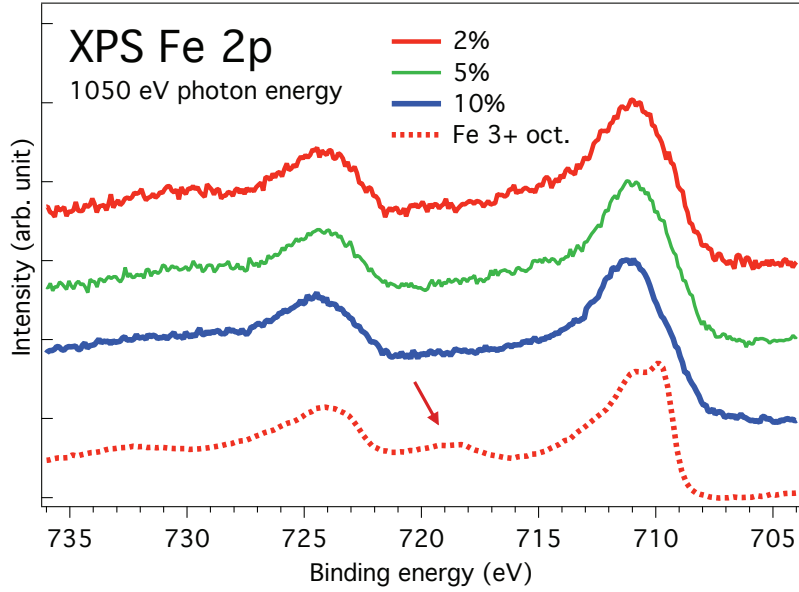


FIG. 1. Fe 2p XPS for different Fe concentrations. A reference Fe³⁺ spectra (red dashed) is also presented. The arrow indicates the location of a satellite structure which can be used for distinguishing between Fe³⁺ and Fe²⁺. All Fe:ZnO spectra indicate a mixed Fe³⁺/Fe²⁺ state.

spectrum represents the non-reduced part for all Fe concentrations and is considered to be a reasonable fit for the bulk since theoretical modeling of magnetometry data gives excellent agreement to experiments by assuming Fe³⁺ in the sample.³⁹ This assumption is also further strengthened in the following sections.

In Fig. 2 we also show the Fe L₃ absorption after different exposure times to x-rays. It is clear that the main peak, which represents Fe³⁺, decreases with time while the peak corresponding to Fe²⁺, increases. This suggests that the Fe³⁺ is reduced in the presence of x-rays. The inset shows the absorption for 5% Fe obtained with both total electron yield (TEY) and partial electron yield (PEY). The PEY is recorded with a micro channel plate (MCP) detector. PEY is more surface sensitive than TEY and the surface sensitivity is further increased by applying a 300 V retarding voltage which blocks the low energy electron generated deeper in the sample. These measurements were performed after about 12 hours of x-ray exposure, hence the sample had reached a steady state with respect to the effect induced by x-rays before conducting the PEY measurements. These measurements reveal that the Fe²⁺/Fe³⁺ ratio is higher closer to the surface than in the bulk.

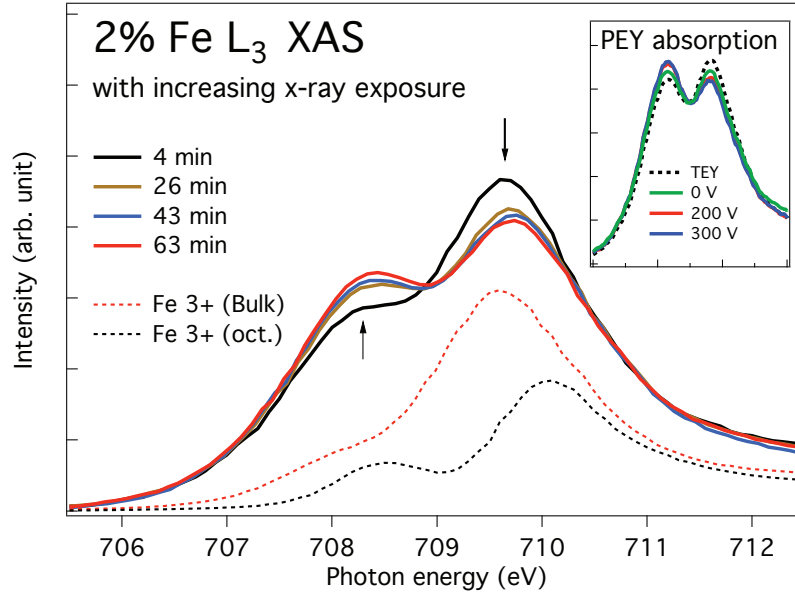


FIG. 2. XAS of 2% Fe:ZnO after different x-ray exposure times. The intensity of the main peak, Fe^{3+} , decreases as the intensity of the pre-edge peak corresponding to Fe^{2+} increases. The inset shows the partial absorption of 5 % Fe obtained after a long x-ray exposure time. The partial absorption indicates that the Fe^{2+} fraction is higher close to the surface.

We have also investigated the sensitivity to x-rays at 700 eV and 730 eV, before and after Fe L_3 absorption respectively, by residing at these photon energies between consecutive Fe L_3 measurements. No significant changes in the reduction of Fe was observed between these photon energies. If the photoionization of Fe were directly involved in the reduction process, then a clear difference should be observed since the photoionization cross-section of Fe 2p is a factor 10-100 larger than for any other Fe core-level at this photon energy range. This suggest that it is likely the x-ray exposure of ZnO which creates oxygen vacancies and reduces the Fe. This is normally difficult to detect since it is not possible to directly measure oxygen vacancies using x-rays and furthermore, Zn almost exclusively exhibits a 2+ oxidation state and can thus not be used for detecting a reduction in ZnO. The creation of oxygen vacancies have been shown to occur in ZnO during UV exposure⁴⁰ which makes these results interesting from a photocatalytic perspective.

B. Quantification of the photoinduced reduction

Quantifying the fraction of Fe^{2+} is not straightforward. Here a simple assumption has been made. The intensity of the pre-edge peak of Fe^{3+} , which contributes to the intensity of Fe^{2+} , is $\frac{1}{3}$ of the main peak (see Fe 3+ (bulk) spectrum in Fig. 2) and equally the intensity of Fe^{2+} contributing to Fe^{3+} is $\frac{1}{3}$ of the main peak.⁴¹ The results are presented in Fig. 3 where all the samples show an increase in the amount of Fe^{2+} as they are subjected to x-rays (note that the time axis is on a logarithmic scale). Interesting to note is the concentration dependence, where the low Fe concentration samples appear more prone to reducing Fe^{3+} upon x-ray exposure. The reduction of the samples is localized to the spot ($1 \times 2 \text{ mm}^2$) where the x-rays are incident. No change in the reduced part of the sample was observed when turning off the x-ray exposure for 60 min. After heating the 2% sample to 400°C it became insensitive to x-ray exposure (dash/rectangles) and there was no difference in absorption between a previously x-ray exposed and non-exposed part of the sample. The sample was then subjected to air after which it showed a similar sensitivity to x-rays as before heating to 400°C . The fraction of Fe^{2+} after heating to 400°C and subsequent air exposure is connected to a saturation of oxygen vacancies and will be discussed further below.

We have calculated the areas under both the XPS Fe $2p_{3/2}$ and XAS Fe L_3 spectra and plotted the corresponding data in Fig. 4 (top) after normalizing with the areas obtained for 1% Fe:ZnO. It is clear that the estimation of the concentration thus obtained does not follow the nominal concentration above 3% Fe:ZnO. The more surface sensitive XPS data shows a lower concentration than XAS at increased Fe concentrations. This can be explained by a surface solubility limit which is reached already around 3% Fe:ZnO. By assuming a simple model where the nominal Fe concentration is only obtained below a 1.4 nm surface layer which has a maximum concentration of 3% Fe, we obtain a good fit to the experimental data, see green and red dashed lines. An electron inelastic mean free path of 1 nm was used for fitting the XPS data which was derived from the 'universal curve' of the electron inelastic mean free path⁴². An electron escape depth of 2.5 nm^{37} was used for modeling the XAS data, which describes the exponential decay of the XAS intensity $I_{XAS} = I_0 \cdot e(-t/2.5)$ as a function of the probing depth t . In Fig. 4 (bottom) we have plotted the Fe^{2+} fraction after 50 min of x-ray exposure obtained from Fig. 3 for different Fe concentrations. Here the fit is obtained using the same model as for the top graph but also including an exponentially decaying

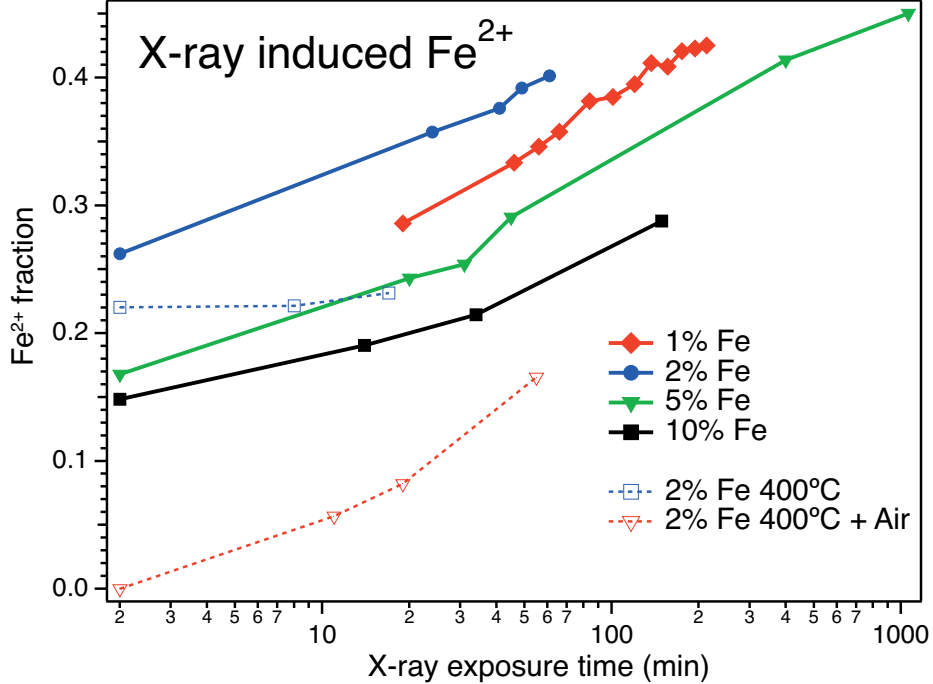


FIG. 3. The fraction of Fe^{2+} obtained from Fe L_3 XAS as a function of the time which the samples are subjected to x-rays. The amount of Fe^{2+} increases with time for all samples.

fraction of Fe^{2+} . The exponential describes a fully reduced surface i.e. $\text{Fe}^{2+}/(\text{Fe}^{2+}+\text{Fe}^{3+})=1$, which decays to $\text{Fe}^{2+}/(\text{Fe}^{2+}+\text{Fe}^{3+})=1/e$ at a depth of 1.4 nm. This model fully describes why we observe an apparent concentration dependence in the susceptibility to reduction by x-rays.

C. Electronic structure at the valence band

The valence band (VB) photoemission spectra of ZnO for different Fe concentrations are given in Fig. 5. The spectra are obtained using a photon energy of 200 eV, except the two spectra denoted 700 eV, which are obtained from resonant photoemission spectra (see Fig. 6). The spectra obtained with 200 eV photon energy are normalized to the same Zn 3d peak height (at ~ 15 eV, not shown). The VB obtained at 700 eV has been normalized to compensate for the change in cross-section ratio of Zn 3d, O 2p and Fe 3d between 200 eV and 700 eV photon energy. The VB of pure ZnO which is mainly comprised of O 2p states has the VB edge at around 3.4 eV binding energy (dashed line) indicating that the Fermi

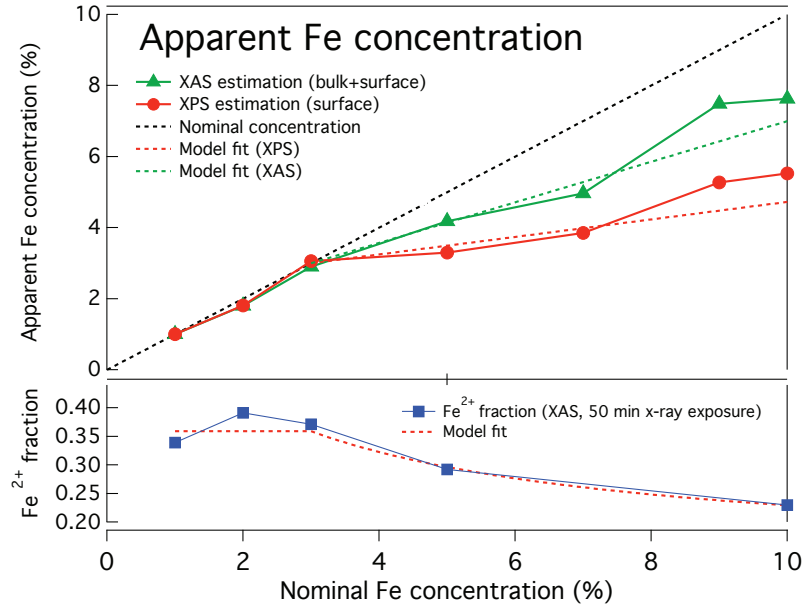


FIG. 4. (Top) The estimated Fe concentration obtained after normalization at 1%Fe:ZnO. The XAS (triangles) estimation is more bulk sensitive than the XPS (circles), suggesting a solubility limit at the ZnO surface of 3% Fe. Dashed lines are fitted by assuming a 1.4 nm surface region with a low Fe concentration. (Bottom) The Fe^{2+} fraction obtained from Fig. 3 after 50 min of x-ray exposure for different concentrations. Dashed line is a model fit assuming an exponential decay length of the Fe reduction of 1.4 nm.

level is located close to the conduction band (CB) edge. The Zn 3d BE for the Fe containing samples are similar as for our pure ZnO, with less than 0.1 eV difference. This behavior is often found for sol-gel produced ZnO.^{43,44} We have aligned the Zn 3d for all samples in Fig. 5 to facilitate the comparison of states in the near band gap region for different samples. Again we emphasize that this only introduces maximum 0.1 eV error in the absolute BE scale.

The lower part of Fig. 5 shows the partial density of states (PDOS) of Fe 3d obtained by subtracting the spectrum of ZnO from the Fe:ZnO samples. The PDOS of the 700 eV measurements should be considered indicative since the VB of pure ZnO, which was used for subtracting, was obtained at 200 eV. The Fe:ZnO sample shows mainly two regions with additional states due to Fe, located in the ZnO bandgap (1 - 2.5 eV BE) and the ZnO VB

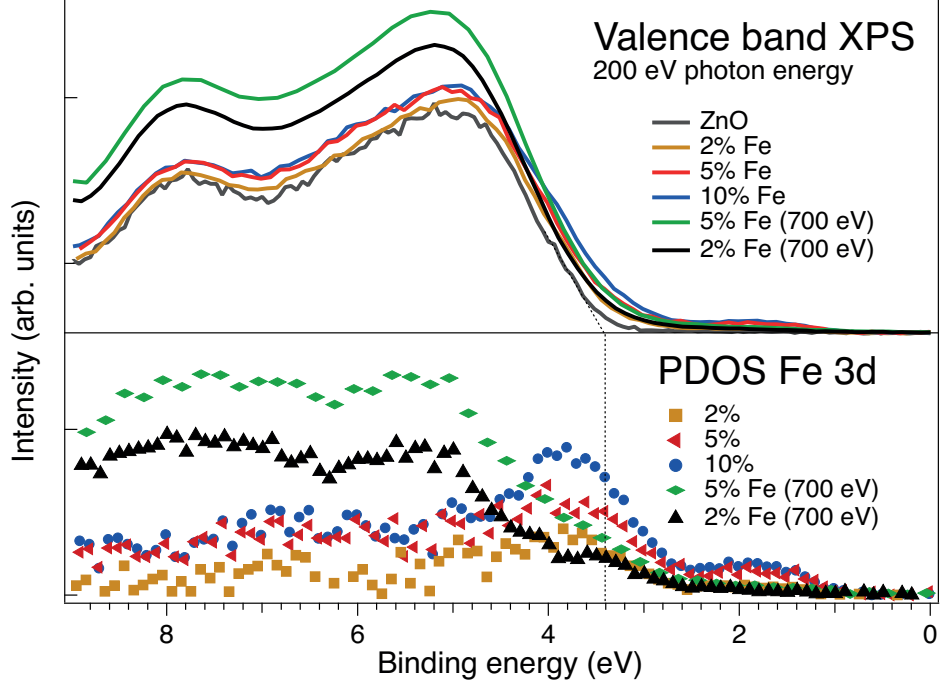


FIG. 5. Valence band photoemission with 200 eV photon energy, except when noted 700 eV. The ZnO has a VB edge at 3.4 eV BE suggesting a Fermi level close to the conduction band. Lower panel shows the partial density of states for Fe 3d. Bandgap states at 2 eV BE are not visible at high photon energies indicating their location on the surface. Fe 3d states are located deeper in the VB for more bulk sensitive measurements using 700 eV photon energy.

edge (2.5 - 4.5 eV BE). These states were also observed by Kataoka et al.³⁷ These spectra were collected with a photon energy of 200 eV but the band gap states are not visible with a photon energy of 700 eV. Lower photon energies gives a higher surface sensitivity which would suggest that the intensity observed in the gap is due to states in the near surface region of the nano-crystals. These states are potentially important for photocatalytic properties and will be discussed further below where we describe the resonant photoemission results. The states observed between 3 and 4 eV BE also appear to have lower intensity at higher photon energies while states located at higher BE than 4 eV have increased.

We have performed resonant photoemission spectroscopy (RPES), see Fig. 6 (right panel), around the Fe L_3 edge to obtain further insight of the states observed in the VB. For photon energies below the Fe L_3 absorption onset, the intensity must formally be due to direct photoemission of valence band states $2p^63d^6 + h\nu \rightarrow 2p^63d^5 + e^-$. At photon energies higher

than the Fe L_3 photoexcitation threshold, there is a second channel available, $2p^63d^6 + h\nu \rightarrow 2p^53d^7 \rightarrow 2p^63d^5 + e^-$, i.e. involving a core hole in the $2p$ level in the intermediate state.⁴⁵ Both channels result in the same final state which gives a resonant enhancement of Fe 3d contribution in the valence band. The main strength of this measurement is that the BE for different chemical states of Fe 3d can be distinguished if they exhibit different absorption energies, which is the case between Fe^{2+} and Fe^{3+} . Also, since the resonant enhancement is closely related to the absorption probability, it is possible to deduce partial absorption spectra which indicates the Fe L_3 absorption structure for different chemical states of Fe.

The partial absorption spectra in Fig. 6 (left panel) are obtained from the RPES data in Fig. 6 (right panel) by integrating the intensity over a specific BE range. A linear background has been subtracted from the partial absorption spectra. The baselines of these spectra have been shifted to coincide with the binding energy of the RPES spectrum to the right, from which the spectra are obtained. The BE integration width was 0.3 eV, centered around the these baselines. The band gap states, which were clearly visible in the valence band spectra in Fig. 5, are now also visible at resonant energies, see spectrum A1. States closer to the the VB edge, see spectrum A4, exhibit a partial absorption which is typical for high spin Fe^{2+} both regarding the peak absorption energy (P2) and the additional shoulder structure.⁴¹ Since spectrum A1 is relatively close to Fe_{HS}^{2+} but shows no multiplet features, it is characterized as Fe_{LS}^{2+} (low-spin).⁴⁶ The crystal field splitting for Fe at the surface, where the Fe^{2+} have been shown to reside, can be very different to what is found in the bulk which could alter the spin state.^{35,47,48} However, it is more likely that the lower coordination on the surface will result in an intermediate spin ($S=1$) state rather than low-spin ($S=0$). We therefore suggest that some of the Fe^{2+} present at the surface are coordinated to a strong ligand such as CO or even O_2 , which have been shown to easily bind to high-spin Fe^{2+} , resulting in a high-spin to low-spin transition.⁴⁹ The spectra A2 and A3 can be modeled by creating suitable linear combinations of A1 and A4. Two peaks, which can not be distinguished here, at photon energies corresponding to P3 and P4 increase in magnitude in spectra A5 to A8. These are attributed to tetrahedrally and octahedrally coordinated Fe^{3+} , respectively.

By choosing a particular photon energy, in the Fe L_3 region, it is possible to isolate different Fe 3d contributions in the VB, as shown in Fig. 7 (left panel). This figure shows the RPES after integrating over different photon energy regions, which are indicated by arrows in Fig. 7 (right panel). A valence band spectrum collected at off-resonance (702 eV) has been

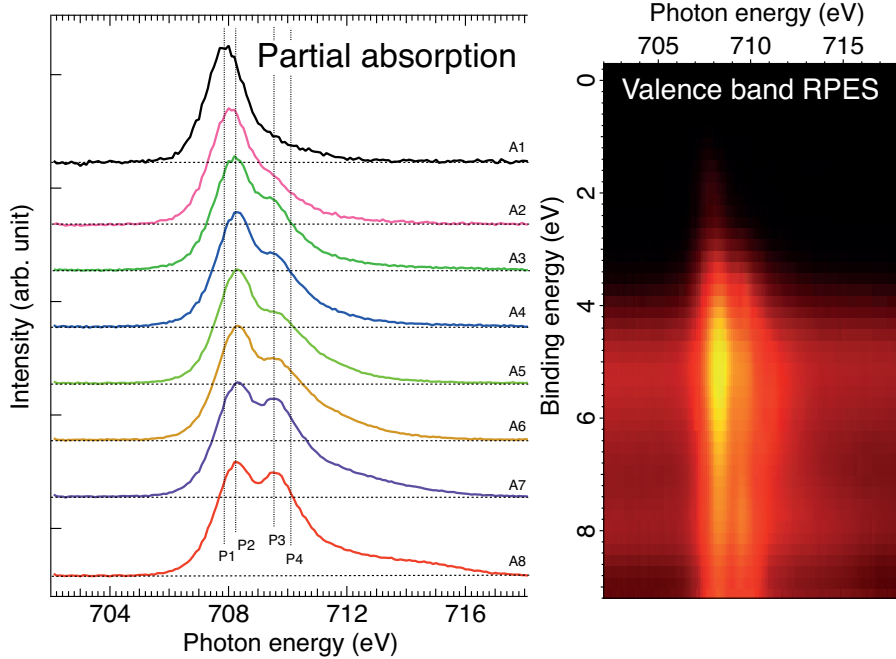


FIG. 6. Partial Fe L_3 absorption (left) and VB RPES (right) of 5% Fe:ZnO. The partial absorption is obtained by taking a slice from the RPES spectrum at the BE corresponding to the base line of the absorption spectra (A1 - A8). Four different components are identified as Fe_{LS}^{2+} , Fe_{HS}^{2+} , Fe^{3+} tetrahedral and Fe^{3+} octahedral with peak positions at P1, P2, P3, and P4, respectively.

subtracted so that the spectra only contain resonant features. The absorption spectrum in Fig. 7 (right panel) is obtained by integrating the 2D spectrum in the right panel of Fig. 6 over the whole binding energy range (0-9 eV binding energy). The intensity of Fe^{2+} compared to Fe^{3+} is much higher than for the TEY signal given in the inset of Fig. 2 due to the surface sensitivity that is established when only electrons that have essentially experienced no inelastic losses are considered. We have already shown that the states located in the ZnO band gap labeled A are due to Fe_{LS}^{2+} , which apparently gives a significant contribution to spectrum S1 in the energy range $\sim 0.5 - 2.4$ eV. However, spectrum S1 also has a contribution from Fe_{HS}^{2+} states. By forming the difference between spectra S1 and S2 we subtract the Fe_{HS}^{2+} component from S1. This difference is shown at the bottom of Fig. 7. By considering the difference spectrum, it is now more clear that features attributed to Fe_{LS}^{2+} states also give intensity at position B, i.e., around 3.6 eV. The BE split between feature A and B is about 1.7 eV which corresponds well to the crystal field splitting induced by a O_2

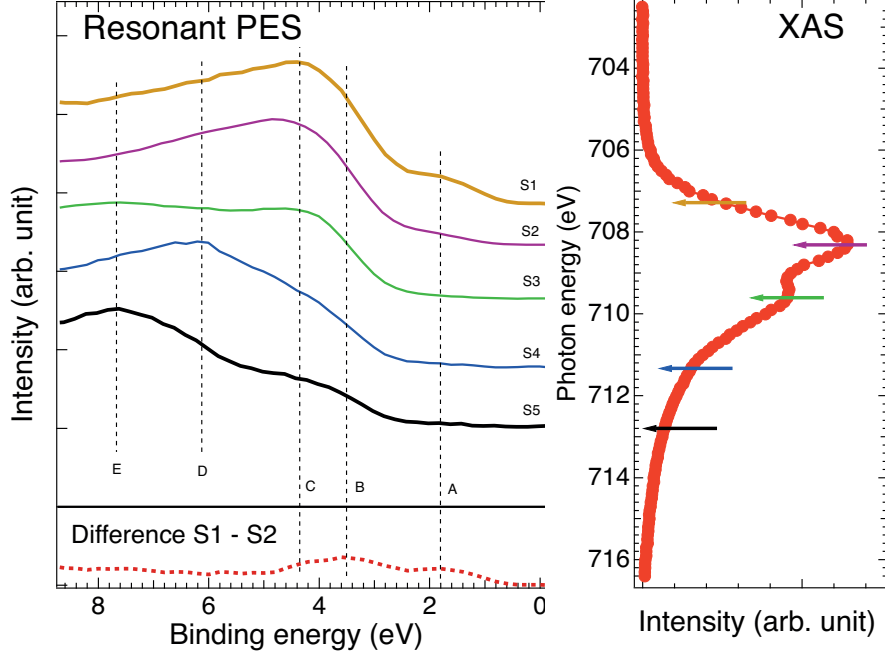


FIG. 7. (Color online) Resonant PES (left) obtained at the photon energies shown in the absorption spectra (right). Resonant features are identified for different valencies and coordinations of Fe ions. The difference between S1 and S2 is shown in the lower part to make feature B more distinct.

ligand.⁴⁹ The S2 spectrum is mainly assigned as being due to Fe_{HS}^{2+} configurations giving the spectral feature at energy position C, though a small contribution from Fe_{LS}^{2+} is not excluded in this energy range. The resonant photoemission spectrum obtained at the excitation energy corresponding to the main Fe^{3+} peak (S3), contains contributions from Fe^{2+} and both Fe^{3+} coordinations, which results in an broad structureless feature. By subtracting a tetrahedral Fe^{3+} component from the partial absorption (not shown) we found that the octahedral and tetrahedral Fe^{3+} components are most easily distinguished using photon energies of 711 eV and 713 eV, respectively. Also, at these photon energies the Fe^{2+} contribution is relatively small. Spectrum S4, recorded with a photon energy in slight excess of 711 eV where we expect to excite predominantly octahedral Fe^{3+} , has most of the intensity at D (~ 6 eV) but shows a feature around C as well. Finally, the spectrum S5 must be mainly attributed to tetrahedral Fe^{3+} since the cross section is small for the other states at these photon energies. Also here, we find a spectral feature deep in the valence band (E) as well as in the valence band edge (B-C). Similar features have been observed by Thurmer et al.⁵⁰ for Fe^{3+}

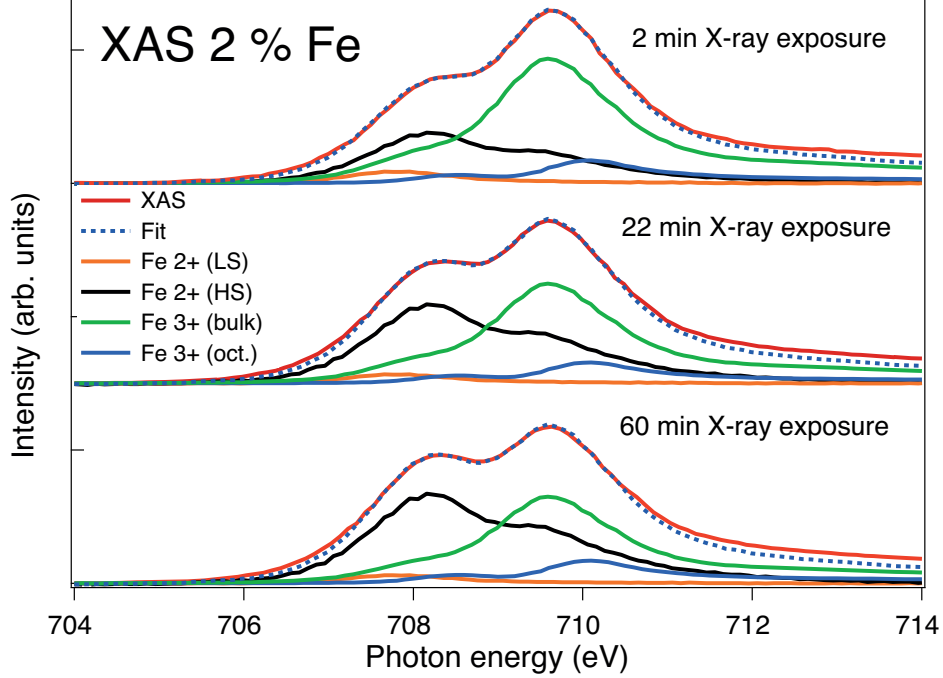


FIG. 8. Decomposition of 2% Fe:ZnO XAS for different x-ray exposure times. The Fe^{3+} (bulk) component decreases with x-ray exposure while the Fe_{HS}^{2+} increases. The other components are relatively weak and appear unaffected by x-ray exposure.

in aqueous solution.

D. Decomposition of Fe 2p and O 1s XAS

The partial absorption spectra A1 (Fe_{LS}^{2+}) and A4 (Fe_{HS}^{2+}) shown in Fig. 6, and the 2% Fe^{3+} bulk spectra and reference Fe^{3+} octahedral spectra in Fig. 2, are used as components for the decomposition of TEY absorption spectra obtained after different x-ray exposures. The bulk Fe^{3+} component decreases with time for the 2% Fe:ZnO samples in Fig. 8, while the Fe_{HS}^{2+} component increases. The Fe_{LS}^{2+} component is very weak as expected since it resides on the surface and TEY is relatively bulk sensitive. It is clear that an additional octahedral Fe^{3+} component is necessary, in excess to the Fe^{3+} (bulk) spectra, for a reasonable fit. Only the Fe_{HS}^{2+} and Fe^{3+} (bulk) appears to be sensitive to x-ray exposure, the intensity is however weak for the other components and the result is thus associated with a large uncertainty. Similar behavior in the decomposition of the 10% Fe:ZnO XAS was also observed (not shown).

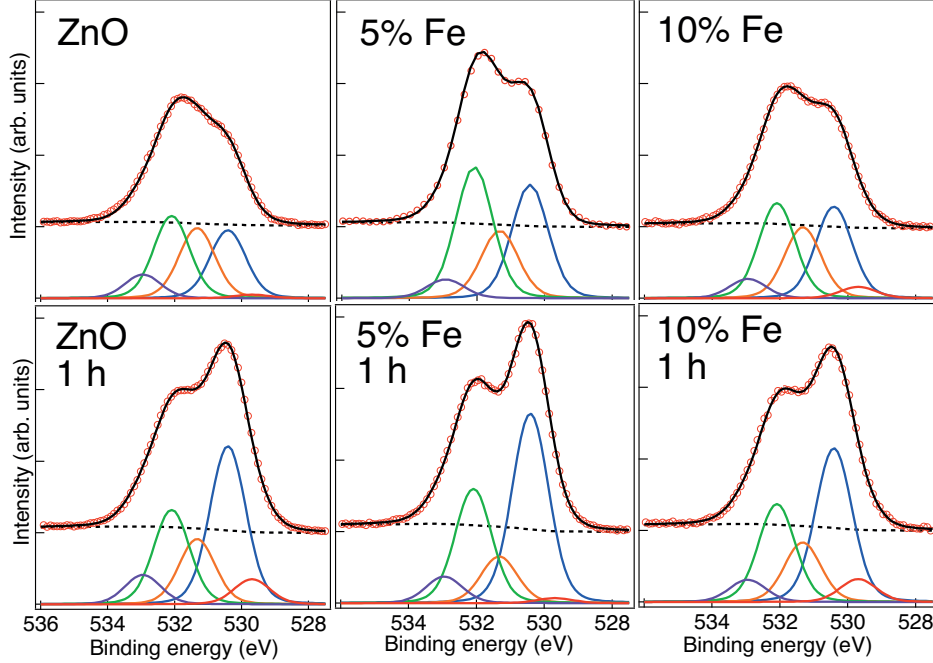


FIG. 9. XPS of O 1s before and after 1 hour of x-ray exposure. The oxygen is fitted by five peaks. Water at high BE (533 eV) is approximately the same for all samples. The hydroxide peak at 532.1 eV is higher for the 5% Fe:ZnO sample but reaches similar levels for all samples after x-ray exposure. The ZnO peak at 530.4 eV is higher for the 5% sample due to less surface adsorbed species.

The deconvoluted spectra of O 1s is shown in Fig. 9 for 10% Fe:ZnO, 5% FeZnO and ZnO. At high binding energy, 533 eV BE, we find O 1s from water with relatively equal intensity between samples, with a small increase after x-ray exposure. The peak at 530.4 eV which is O^{2-} from the ZnO wurtzite structure becomes more visible as the surface layer of carbon is partly desorbed by x-ray exposure. The total amount of carbon is about 12% lower for the 5% Fe:ZnO sample (not shown) than for the other two samples which can explain why the O^{2-} peak is more visible for the 5% Fe:ZnO sample. However, after 1 hour of x-ray exposure the average carbon intensity decrease is 20% after which the carbon content is about the same for all samples. The peaks at 532.1 eV and 531.3 eV BE are both in the range of hydroxyl and are likely species bound to different sites at the surface.^{8,16,51,52} The weak structure at 529.7 eV BE is not found in the literature, probably since it is difficult to resolve from the main peak at 530.4 eV BE.^{16,52,53} This peak is only observed for 10%

Fe:ZnO and ZnO and could be related to a small shift in the Zn 3d peak of 70 meV to lower BE after 1 hour of x-ray exposure since both effects are observed for the pure ZnO and 10% Fe:ZnO sample but not for the 5% Fe:ZnO sample. Due to the large difference in the observed shift between Zn and O it cannot be related to a Fermi level shift. However, a large increase in the number of available charge carriers induced by oxygen vacancies could improve the screening of the core ionized final state, resulting in a chemical shift to lower BE for both O and Zn. As was mentioned earlier, oxygen vacancies which are generated by the x-ray exposure are likely responsible for the reduction of Fe. The 2% sample becomes insensitive to x-ray exposure after heat treatment to 400°C, see Fig. 3, since oxygen vacancies already are induced by heating to the extent that further creation by irradiation is unfavorable.^{54,55} The Fe²⁺ component does not show the same intensity asymmetry between PEY and TEY absorption after heating to 400°C as before heating, indicating the existence of oxygen vacancies deeper in the bulk of the ZnO. Also, since heating generates more oxygen vacancies overall (bulk and surface), a relatively speaking smaller amount can be generated near the surface before additional creation of vacancies becomes unfavorable. This could explain the lower fraction of Fe²⁺ obtained for the 400°C heat treated sample. Exposing this sample to air, removes oxygen vacancies and it again becomes sensitive to x-ray exposure, see Fig. 3.

Both CO₂ and hydroxide binds to oxygen vacancies on the ZnO surface^{52,56,57} which can explain the lower amount of carbon on the 5% Fe:ZnO sample. An intermediate concentration of Fe will make the surface more prone to bind OH instead of CO₂. Increased OH peaks have been connected to increased photocatalytic performance.^{16,53} We also observe that the decrease of the OH peaks when exposed to x-rays is larger for the 5%Fe:ZnO sample in accordance with the finding that intermediate doping of transition metal in ZnO can increase the production of hydroxide radicals in photocatalytic processes.^{8,17}

The O 1s spectra in Fig. 9 were collected without heating the sample to 220°C since both the carbon and oxygen spectra are insensitive to x-ray exposure after heating. The Fe spectra are relatively unaffected by the heat treatment which means that the creation of oxygen vacancies is not only induced by the desorption of surface adsorbates.

IV. CONCLUSIONS

An detailed study of Fe:ZnO for Fe concentrations in the range 1-10 % have been performed by means of x-ray photoemission spectroscopy and x-ray absorption spectroscopy. The bulk is found to contain mainly Fe^{3+} in octahedral and tetrahedral coordination. An amorphous $\text{Zn}_x\text{Fe}_y\text{O}$ was found with Raman spectroscopy and TEM, whereas XRD suggests a pure ZnO wurtzite structure. We have observed a high sensitivity to x-rays in the surface composition of Fe. Fe^{3+} in the near surface region is reduced to Fe^{2+} by x-ray exposure. The reduction appears insensitive to the energy of the x-rays suggesting that the effect is not connected to the photoionization of the Fe atom. We believe the reduction to occur due to the creation of oxygen vacancies. Since the creation of oxygen vacancies have been shown to occur in ZnO during UV exposure⁴⁰, the results obtained here are likely very relevant for photocatalytic properties in ZnO. The reduction is not due to the desorption of any adsorbed molecules since the reduction of Fe prevails even though the C 1s and O 1s XPS are unaffected by x-rays after heat treatment to 220°C. Since there is no apparent surface preference of Fe^{2+} after heating to 400°C we can conclude that the reduction occurs deeper inside the sample by heat treatment than by x-ray exposure. A model which suggests the reduction to occur down to about 1.4 nm below the surface fits well with the experimental data. We have shown that the solubility of Fe is only about 3 % in this region, which is a likely explanation to the finding that the photocatalytic efficiency peaks at low doping concentrations. We propose that it is only dopant atoms associated to the surface region which have a positive effect on the catalytic properties. Sample preparations methods that can increase the surface concentration of Fe while keeping the concentration low in the bulk can thus give a significant increase of the catalytic efficiency of ZnO. We have also found that an intermediate Fe concentration seems to promote hydroxide adsorbents rather than CO_2 and is more sensitive to x-rays concerning the desorption of hydroxide. This is in contrast to the high Fe concentration sample which is very similar to pure ZnO in these aspects, which could explain why the photocatalytic efficiency decreases for high doping concentrations.

Valence band XPS shows Fe states deep in the ZnO bandgap as well as states at the VB edge. Resonant photoemission indicates the BE position of Fe 3d states for different Fe constituents. States associated to Fe^{2+} are found at the VB edge, while the Fe^{3+} components correspond to spectral features also at higher BE. The bandgap states are proposed to be

Fe²⁺ in a low-spin configuration. The low-spin state is likely formed by a ligand such as O₂ which increases the crystal field splitting. These states are formed at the surface and are potentially very important for visible light photocatalytic activity due to their location deep in the VB, which makes it possible to induce electron-hole pairs with visible light.

ACKNOWLEDGMENTS

The authors thank Swedish scientific council (VR), the Foundation for Strategic Research (SSF), and the Göran Gustafsson Foundation for financial support. R. K. would like to thank A. Schaefer and M. Webb for useful discussions. The support of the MAX-lab staff, A. Preobrajenskij is gratefully acknowledged.

-
- ¹ H. Yan, J. Hou, Z. Fu, B. Yang, P. Yang, K. Liu, M. Wen, Y. Chen, S. Fu, and F. Li, *Materials Research Bulletin*, **44**, 1954 (2009).
 - ² M. Muruganandham, N. Shobana, and M. Swaminathan, *Journal of Molecular Catalysis A: Chemical*, **246**, 154 (2006).
 - ³ S. Sakthivel, B. Neppolian, M. V. Shankar, B. Arabindoo, M. Palanichamy, and V. Murugesan, *Solar Energy Materials and Solar Cells*, **77**, 65 (2003).
 - ⁴ R. Asahi, T. Morikawa, T. Ohwaki, K. Aoki, and Y. Taga, *Science*, **293**, 269 (2001).
 - ⁵ E. Casbeer, V. K. Sharma, and X.-Z. Li, *Separation and Purification Technology*, **87**, 1 (2012).
 - ⁶ S. Ekambaram, Y. Iikubo, and A. Kudo, *Journal of Alloys and Compounds*, **433**, 237 (2007).
 - ⁷ Z. Zou, J. Ye, K. Sayama, and H. Arakawa, *Nature*, **414**, 625 (2001).
 - ⁸ H. Bai, Z. Liu, and D. D. Sun, *Phys. Chem. Chem. Phys.*, **13**, 6205 (2011).
 - ⁹ R. Wang, K. Hashimoto, A. Fujishima, M. Chikuni, E. Kojima, A. Kitamura, M. Shimohigoshi, and T. Watanabe, *Nature*, **388**, 431 (1997).
 - ¹⁰ Z. Zhang, H. Chen, J. Zhong, G. Saraf, and Y. Lu, *Journal of Electronic Materials*, **36**, 895 (2007).
 - ¹¹ E. L. Papadopoulou, M. Barberoglou, V. Zorba, A. Manousaki, A. Pagkozidis, E. Stratakis, and C. Fotakis, *Journal of Physical Chemistry C*, **113**, 2891 (2009).
 - ¹² R.-D. Sun, A. Nakajima, A. Fujishima, T. Watanabe, and K. Hashimoto,

- Journal of Physical Chemistry B, **105**, 1984 (2001).
- ¹³ M. Miyauchi, N. Kieda, S. Hishita, T. Mitsuhashi, A. Nakajima, T. Watanabe, and K. Hashimoto, *Surface Science*, **511**, 401 (2002).
- ¹⁴ S. Rehman, R. Ullah, A. M. Butt, and N. D. Gohar, *Journal of Hazardous Materials*, **170**, 560 (2009).
- ¹⁵ “Only 5% of the total energy from the sun is in the UV region while 46% corresponds to visible light and 49% is in the infrared region.”.
- ¹⁶ M. Fu, Y. Li, S. Wu, P. Lu, J. Liu, and F. Dong, *Applied Surface Science*, **258**, 1587 (2011).
- ¹⁷ C.-Y. Kao, J.-D. Liao, C.-W. Chang, and R.-Y. Wang, *Applied Surface Science*, **258**, 1813 (2011).
- ¹⁸ Q. Xiao, J. Zhang, C. Xiao, and X. Tan, *Materials Science and Engineering: B*, **142**, 121 (2007).
- ¹⁹ J. Yu, M. Zhou, H. Yu, Q. Zhang, and Y. Yu, *Materials Chemistry and Physics*, **95**, 193 (2006).
- ²⁰ T. Zubkoy, D. Stahl, T. L. Thompson, D. Panayotov, O. Diwald, Y. Jr., and J.T., *Journal of Physical Chemistry B*, **109**, 15454 (2005).
- ²¹ S. Xu, D. Feng, and W. Shangguan, *The Journal of Physical Chemistry C*, **113**, 2463 (2009).
- ²² P. Cheng, C. Deng, M. Gu, and W. Shangguan, *Journal of Materials Science*, **42**, 9239 (2007).
- ²³ K.-Z. Zhang, B.-Z. Lin, Y.-L. Chen, B.-H. Xu, X.-T. Pian, J.-D. Kuang, and B. Li, *Journal of Colloid and Interface Science*, **358**, 360 (2011).
- ²⁴ S. Boumaza, A. Boudjemaa, A. Bouguelia, R. Bouarab, and M. Trari, *Applied Energy*, **87**, 2230 (2010).
- ²⁵ J. Xia, A. Wang, X. Liu, and Z. Su, *Applied Surface Science*, **257**, 9724 (2011).
- ²⁶ M. A. Valenzuela, P. Bosch, J. Jiménez-Becerrill, O. Quiroz, and A. I. Páez, *Journal of Photochemistry and Photobiology A: Chemistry*, **148**, 177 (2002).
- ²⁷ N. V. Kaneva and C. D. Dushkin, *Colloids and Surfaces A: Physicochemical and Engineering Aspects*, **382**, 211 (2011).
- ²⁸ Q. Xiao and C. Yao, *Materials Chemistry and Physics*, **130**, 5 (2011).
- ²⁹ S. Dong, K. Xu, J. Liu, and H. Cui, *Physica B: Condensed Matter*, **406**, 3609 (2011).
- ³⁰ Dongwoon and Jung, *Solid State Sciences*, **12**, 466 (2010).
- ³¹ C. Woll, *Progress in Surface Science*, **82**, 55 (2007).
- ³² U. Kvist, M. Ottosson, A. Hoffmann, P. Svedlind, R. Knut, O. Karis, W. Wan, X. Zou, and A. Pohl, to be published.

- ³³ A. P. Grosvenor, B. A. Kobe, M. C. Biesinger, and N. S. McIntyre, *Surface and Interface Analysis*, **36**, 1564 (2004).
- ³⁴ P. C. J. Graat and M. A. J. Somers, *Applied Surface Science*, **100-101**, 36 (1996).
- ³⁵ T. Droubay and S. A. Chambers, *Phys. Rev. B*, **64**, 205414 (2001).
- ³⁶ T. Yamashita and P. Hayes, *Applied Surface Science*, **254**, 2441 (2008).
- ³⁷ T. Kataoka, M. Kobayashi, Y. Sakamoto, G. S. Song, A. Fujimori, F.-H. Chang, H.-J. Lin, D. J. Huang, C. T. Chen, T. Ohkochi, Y. Takeda, T. Okane, Y. Saitoh, H. Yamagami, A. Tanaka, S. K. Mandal, T. K. Nath, D. Karmakar, and I. Dasgupta, *Journal of Applied Physics*, **107** (2010).
- ³⁸ G. der Laan and I. W. Kirkman, *J. Phys.: Condensed Matter*, **4**, 4189 (1992).
- ³⁹ R. Knut, U. Kvist, A. Pohl, O. Karis, B. Sanyal, and P. Svedlind, to be published.
- ⁴⁰ Q. H. Li, T. Gao, Y. G. Wang, and T. H. Wang, *Applied Physics Letters*, **86**, 123117 (2005).
- ⁴¹ R. G. Wilks, E. Z. Kurmaev, J. C. Pivin, A. Hunt, M. V. Yablonskikh, D. A. Zatsepin, A. Moewes, S. Shin, P. Palade, and G. Principi, *Journal of Physics Condensed Matter*, **17**, 7023 (2005).
- ⁴² M. P. Seah and W. A. Dench, *Surface and Interface Analysis*, **1**, 2 (1979), ISSN 1096-9918.
- ⁴³ D. Iusan, R. Knut, B. Sanyal, O. Karis, O. Eriksson, V. A. Coleman, G. Westin, J. M. Wikberg, and P. Svedlindh, *Phys. Rev. B*, **78**, 85319 (2008).
- ⁴⁴ R. Knut, J. M. Wikberg, K. Lashgari, V. A. Coleman, G. Westin, P. Svedlindh, and O. Karis, *Phys. Rev. B*, **82**, 94438 (2010).
- ⁴⁵ P. A. Brühwiler, O. Karis, and N. Mårtensson, *Reviews of Modern Physics*, **74**, 703 (2002), ISSN 00346861.
- ⁴⁶ H. Wang, G. Peng, L. M. Miller, E. M. Scheuring, S. J. George, M. R. Chance, and S. P. Cramer, *Journal of the American Chemical Society*, **119**, 4921 (1997).
- ⁴⁷ M. Bronold, Y. Tomm, and W. Jaegermann, *Surface Science*, **314**, L931 (1994).
- ⁴⁸ H. W. Nesbitt, M. Scaini, H. Höchst, G. M. Bancroft, A. G. Schaufuss, and R. Szargan, *American Mineralogist*, **85**, 850 (2000).
- ⁴⁹ D. Benito-Garagorri, I. Lagoja, L. F. Veiros, and K. A. Kirchner, *Dalton Transactions*, **40**, 4778 (2011).
- ⁵⁰ S. Thürmer, R. Seidel, W. Eberhardt, S. E. Bradforth, and B. Winter, *Journal of the American Chemical Society*, **133**, 12528 (2011).

- ⁵¹ S. Sepulveda-Guzman, B. Reeja-Jayan, E. de la Rosa, A. Torres-Castro, V. Gonzalez-Gonzalez, and M. Jose-Yacaman, *Materials Chemistry and Physics*, **115**, 172 (2009).
- ⁵² M. Kunat, S. Girol, U. Burghaus, and C. Wöll, *Journal of Physical Chemistry B*, **107**, 14350 (2003).
- ⁵³ L. Jing, B. Xin, F. Yuan, L. Xue, B. Wang, and H. Fu, *Journal of Physical Chemistry B*, **110**, 17860 (2006).
- ⁵⁴ M. Rusop, K. Uma, T. Soga, and T. Jimbo, *Materials Science and Engineering: B*, **127**, 150 (2006).
- ⁵⁵ T. Hiramatsu, M. Furuta, T. Matsuda, C. Li, and T. Hirao, *Applied Surface Science*, **257**, 5480 (2011).
- ⁵⁶ C. T. Au, W. Hirsch, and W. Hirschwald, *Surface Science*, **197**, 391 (1988).
- ⁵⁷ R. Lindsay, E. Michelangeli, B. G. Daniels, T. V. Ashworth, A. J. Limb, G. Thornton, A. Gutiérrez-Sosa, A. Baraldi, R. Larciprete, and S. Lizzit, *Journal of the American Chemical Society*, **124**, 7117 (2002).